SCIENCE CHINA Materials ARTICLES

mater.scichina.com link.springer.com

Published online 29 July 2021 | https://doi.org/10.1007/s40843-021-1706-4
Sci China Mater 2021, 64(12): 3101–3113

NIR-absorbing superoxide radical and hyperthermia photogenerator *via* twisted donor-acceptor-donor molecular rotation for hypoxic tumor eradication

Yucheng Zhu[1†], Qinghua Wu[2†], Chao Chen[1], Guoliang Yang[1], Hongliang Cao[1], Yun Gao[1], Lijuan Jiao[2*], Erhong Hao[2*] and Weian Zhang[1*]

ABSTRACT **Hypoxia severely impedes the therapeutic efficacies of tumor chemotherapy, radiotherapy and conventional photodynamic therapy (type II PDT). Herein, we proposed a nonplanar near-infrared (NIR)-absorbing hyperthermia and superoxide radical ($O_2^{-\bullet}$) photogenerator (TB) against hypoxic tumors. TB particularly possessed a favorable $O_2^{-\bullet}$ generation capability under 808 nm laser irradiation with the donor-acceptor-donor (D-A-D) molecular structure. Moreover, owing to molecular rotation, potent hyperthermia was realized under continuous laser irradiation. For the usage of hypoxic tumor treatment, TB was encapsulated by a block copolymer, poly(ethylene glycol)-*b*-poly(latic acid) (PEG_{45}-*b*-PLA_{24}), to fabricate phototheranostic nanoparticles (TB NPs). Due to the twisted molecular structure and the shielding effect of long alkyl chains, the π-π stacking-induced quenching of $O_2^{-\bullet}$ could be reduced after the fabrication of nano-assemblies. Significantly, TB NPs exhibited satisfactory $O_2^{-\bullet}$ generation for type I PDT and a simultaneously distinct photothermal conversion efficiency (PCE, 62%) for photothermal therapy (PTT) to combat hypoxic tumor cells. Moreover, the high PCE endowed TB NPs with high-performance photoacoustic (PA) and photothermal imaging capability. *In vivo* experiments demonstrated that TB NPs possessed an outstanding phototherapeutic efficacy for eradicating hypoxic tumors. This study established a novel approach for constructing oxygen-independent phototherapeutic reagent against hypoxic tumors.**

Keywords: tumor hypoxia, superoxide radical, hyperthermia, D-A-D structure, molecular rotation

INTRODUCTION

Hypoxia, a remarkable feature in tumor microenvironments, is one of the major factors limiting the therapeutic efficacies of tumor chemotherapy, radiotherapy and conventional photodynamic therapy (type II PDT) [1–6]. To eliminate the negative influence of hypoxia during treatment, some innovative measures have been adopted, such as hyperbaric oxygen therapy, the introduction of external-oxygen carriers (e.g., perfluorocarbon and hemoglobin), *in situ* O_2-generated catalysts (e.g., photosynthetic bacteria and catalase) and/or O_2 suppliers (e.g., CaO_2) [7–19]. Although these approaches have made significant progress, they often need the introduction of new O_2 enrichment materials or complicated processes. Thus, it is promising to develop oxygen-independent therapeutics.

Superoxide radical ($O_2^{-\bullet}$) has been recognized as one of the main oxidants for cancer therapeutics because of its ability to arouse DNA chain breakage, membrane injury and mitochondrial oxidative phosphorylation [20–24]. For example, excessive mitochondrial $O_2^{-\bullet}$ could trigger autophagy-induced cell apoptosis [25,26]. Additionally, under the intracellular superoxide dismutase (SOD)-mediated disproportionation reactions, $O_2^{-\bullet}$ could further convert downstream into highly toxic hydroxyl radical (·OH) to aggravate the anticancer efficacy [27–29]. In the previous research, $O_2^{-\bullet}$ could be produced for cancer therapies by some inorganic or organic reagents under light irradiation, and thus this $O_2^{-\bullet}$-based PDT (type I PDT) is a potential cancer treatment for merits of non-

[1] Shanghai Key Laboratory of Functional Materials Chemistry, School of Materials Science and Engineering, East China University of Science and Technology, Shanghai 200237, China
[2] Laboratory of Functional Molecular Solids, Ministry of Education, Anhui Laboratory of Molecule Based Materials (State Key Laboratory Cultivation Base) and School of Chemistry and Materials Science, Anhui Normal University, Wuhu 241000, China
† These authors contributed equally to this work.
* Corresponding authors (emails: jiao421@ahnu.edu.cn (Jiao L); haoehong@ahnu.edu.cn (Hao E); wazhang@ecust.edu.cn (Zhang W))

invasiveness, low systemic-toxicity and high selectivity. In comparison with inorganic $O_2^{-\bullet}$ generators (e.g., metal-oxide nanoparticles (NPs) and metal-organic frameworks) [30–33], organic $O_2^{-\bullet}$ photogenerators have attracted extensive attention due to their biodegradability and reduced pharmacokinetic complexity. Despite the tremendous advances, there is remarkable scope to improve the performance of organic $O_2^{-\bullet}$ photogenerators. For example, the inherent defects of most $O_2^{-\bullet}$ photogenerators, such as short maximum absorption wavelength (less than 750 nm) and poor photo/chemical stability, would limit the therapeutic efficacy against deep tumors [34,35]. Moreover, normal nonplanar $O_2^{-\bullet}$ photogenerators tend to aggregate in physiological environments which might induce the quenching of $O_2^{-\bullet}$ [36,37]. Based on the above considerations, it is highly desired to fabricate a nonplanar near-infrared (NIR)-absorbing $O_2^{-\bullet}$ photogenerator.

As another oxygen-independent phototherapy, photothermal therapy (PTT) *via* laser-triggered photothermal reagents has been intensively explored in defeating hypoxic tumors [38]. For PTT, a vital factor is the photothermal conversion efficiency (PCE) which primarily depends on the internal conversion of photothermal reagents [39]. The commonly used strategies for enhancing PCE of photothermal reagents are the π-π stacking of planar molecules and the conjugation of small molecules [40–44]. To design photothermal photogenerators with higher PCE, it is favorable to introduce a molecular rotor to luminogens, in which the molecular motion in their aggregates could be greatly boosted, resulting in distinct PCE [45–50]. Nevertheless, rare efforts have been dedicated on developing highly photostable photothermal reagents with high PCE and large molar extinction coefficient at long irradiation wavelengths (e.g., 808 nm). Additionally, high cancer therapeutic efficacies could be achieved by the synergistic treatment of PTT with other therapeutic modalities [51–55]. In particular, several studies revealed that PTT showed an enhancement to the PDT efficacy for its ability to increase the blood flow rate [56–58]. Toward this end, it is desirable to integrate hyperthermia into a robust $O_2^{-\bullet}$ photogenerator so as to develop a powerful oxygen-independent phototherapeutic reagent against hypoxic tumors.

Herein, we developed an ideal $O_2^{-\bullet}$ and hyperthermia photogenerator (**TB**) to fill the gap through engineering the twisted donor-acceptor-donor (D-A-D) conjugated structure against hypoxic tumors (Scheme 1). Specifically, by the introduction of long alkyl chains-substituted tetraphenylethene unit ($C_{12}H_{25}$OTPE, as a molecular rotor and electron donor) to dimer BODIPY core, **TB** possessed the following advantageous characteristics: (i) maximum absorption at 802 nm and the extremely huge peak mass extinction coefficient (286.57 L g^{-1} cm^{-1}) could efficiently help **TB** trap NIR photons; (ii) ultra-stable photostability made **TB** a suitable phototheranostic reagent under continuous irradiation; (iii) the twisted D-A-D molecular structure not only facilitated electron transfer but also prevented the intermolecular π-π stacking, which enhanced the $O_2^{-\bullet}$ generation under irradiation; (iv) molecular rotation between the $C_{12}H_{25}$ OTPE unit and dimer BODIPY core endowed **TB** with ultrahigh photothermal conversion (Scheme 1a). The detailed generation mechanism of $O_2^{-\bullet}$ and hyperthermia was fully revealed by theoretical calculation. This is the first time for designing such a delicate unimolecular $O_2^{-\bullet}$ plus hyperthermia photogenerator with such a long absorption wavelength. Furthermore, for hypoxic tumor treatment, **TB** NPs were fabricated *via* the encapsulation of **TB** with a block copolymer, poly(ethylene glycol)-*b*-poly(latic acid) (PEG_{45}-*b*-PLA_{24}) [59]. Owing to the superior photophysical properties of **TB**, *in vivo* experiments have disclosed that **TB** NPs possessed an outstanding type I PDT efficacy for tumor suppression. Completely hypoxic tumor eradication was observed for **TB** NPs under synergistic type I PDT/PTT treatment (Scheme 1b).

EXPERIMENTAL SECTION

Materials

Reagents and solvents were purchased from Energy Chemicals except 9,10-anthracenediyl-bis(methylene)-dimalonic acid (ABDA), 5,5-dimethyl-1-pyrroline-1-oxide (DMPO), singlet oxygen sensor green (SOSG), dihydroethidium (DHE), hydroxyphenyl fluorescein (HPF), annexin V-fluorescein isothiocyanate (FITC) and propidium iodide (PI) purchased from Beyotime Institute of Biotechnology.

Synthesis and characterization of TB

The synthesis of **TB** is depicted in the Supplementary information. ^{1}H nuclear magnetic resonance (NMR), ^{13}C NMR and matrix-assisted laser desorption/ionization-time of flight (MALDI-TOF) were used for the characterization of **TB**. ^{1}H NMR (400 MHz, $CDCl_3$): δ 7.85 (d, J = 8.2 Hz, 1H), 7.20–7.05 (m, 3H), 7.03–6.92 (m, 2H), 6.65 (m, J = 8.6, 7.5 Hz, 2H), 6.60 (d, J = 4.3 Hz, 1H), 6.57 (d, J = 4.5 Hz, 1H), 3.88 (m, J = 15.3, 6.6 Hz, 1H), 2.40 (s, 1H), 2.16 (s, 2H), 1.72 (m, J = 21.4, 14.7, 6.8 Hz, 1H),

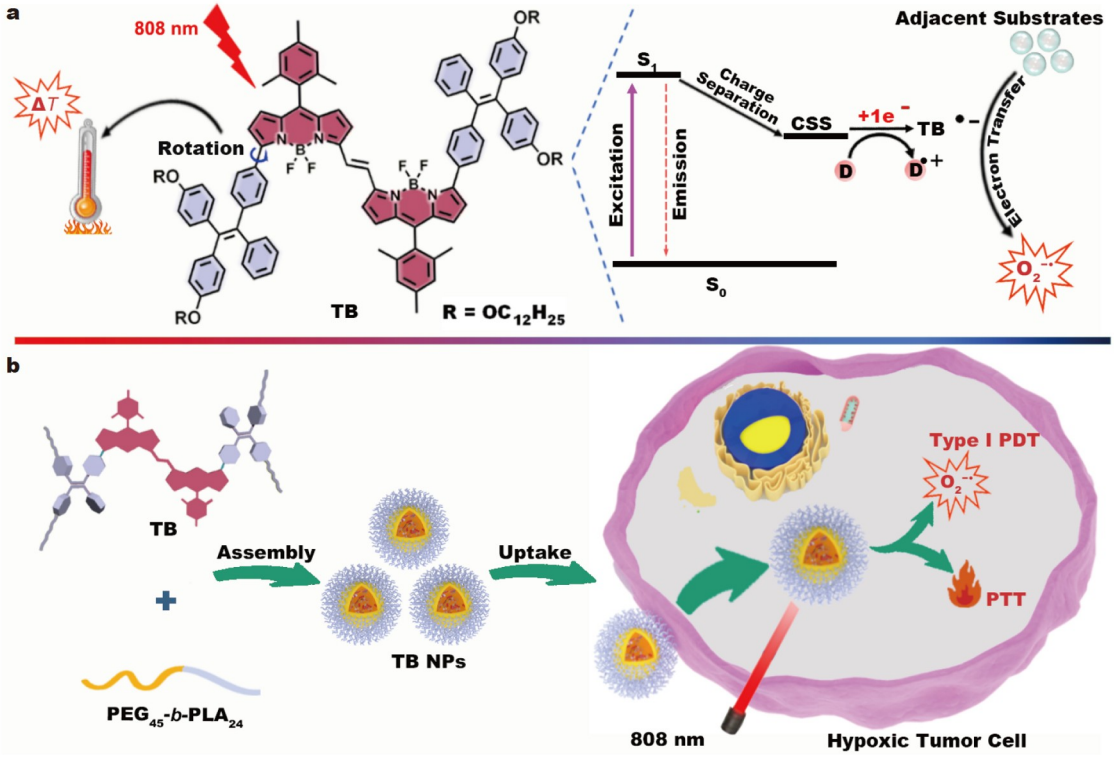

Scheme 1 (a) Chemical structure of the probable mechanism of $O_2^{-\bullet}$ and hyperthermia generation for **TB** under 808 nm laser illumination (S_0: ground state; S_1: singlet excited state; CSS: charge-separated state; D: electron donor). (b) Scheme illustration of the fabricated **TB** NPs against hypoxic tumor cells.

1.50–1.16 (m, 12H), 0.90 (q, J = 6.9 Hz, 2H). ^{13}C NMR (101 MHz, $CDCl_3$) δ 157.99, 157.77, 146.12, 144.10, 141.43, 140.26, 138.49, 137.98, 137.22, 136.89, 136.11, 135.91, 132.67, 131.65, 131.49, 130.29, 129.64, 129.17, 128.92, 128.16, 127.76, 126.16, 113.67, 113.49, 77.33, 77.01, 76.70, 67.83, 31.92, 31.91, 29.67, 29.64, 29.63, 29.60, 29.59, 29.58, 29.56, 29.43, 29.35, 29.34, 29.31, 29.29, 26.07, 26.04, 22.70, 22.69, 21.16, 20.08, 14.13. High-resolution mass spectrometer (HRMS) (MALDI-TOF) m/z: $[M]^+$ calculated for $C_{138}H_{166}B_2F_4N_4O_4$ 2042.3080, found 2042.3083.

Preparation of TB NPs and ICG-labelled TB NPs

Preparation of **TB** NPs: **TB** (1 mg) and PEG_{45}-*b*-PLA_{24} (15 mg) were first dissolved in 1 mL tetrahydrofuran (THF), and then the solution was slowly added into 4 mL phosphate buffer saline (PBS, pH 7.4) under intense stirring. Afterwards, the solution was stirred for 2 h and dialyzed for further usage.

Preparation of indocyanine green (ICG)-labelled **TB** NPs: Briefly, 1 mg ICG, 1 mg **TB** and 15 mg PEG_{45}-*b*-PLA_{24} were dissolved in 1 mL THF, and the solution was then added dropwise into 4 mL PBS (pH 7.4). The solution was dialyzed against ultrapure water in a dialysis bag (molecular weight cut-off 3500) for three days at room temperature. ICG-labelled **TB** NPs were then obtained after dialysis.

Cell viability for TB NPs

For *in vitro* phototoxicity, 4T1 and MCF-7 cells (25,000 cells mL^{-1}, 200 μL) were cultivated into 96-well plates for 24 h. Then the culture medium was replaced by new culture medium containing **TB** NPs. After the cells were cultured for another 24 h, they were irradiated for 5 min (0.25 W cm^{-2}) and incubated for another 8 h. Thereafter, the fresh culture medium with 20 μL methyl thiazolyl-tetrazolium (MTT) (5 mg mL^{-1}) was used to replace the original culture medium for a further incubation of 4 h. Finally, the culture medium was removed and 150 μL dimethyl sulfoxide (DMSO) was added into each well, followed by measuring the absorbance at 492 nm on a spectrophotometric microplate reader. To evaluate the cell cytotoxicity under hypoxia, the 4T1 cells were firstly cultured in a 96-well cell plate in the 21% O_2 atmosphere for 24 h, and further cultured in a 2% O_2 atmosphere for another 8 h. Then, the following proce-

dure was similar to that in normoxia except the cultivation conditions.

Animal experiments

All animal procedures were performed in accordance with the Chinese legislation on the Use and Care of Research Animals (Document No. 55, 2001), and institutional guidelines for the Care and Use of laboratory animals established by the East China University of Science and Technology Animal Studies Committee, and this committee approved the experiments.

Female nude mice (4 to 6 weeks old) were placed in the pathogen-free environment (24°C). The mice were injected with 100 μL cell suspension containing 5×10^6 4T1 cells. Then the mice were randomized into five groups, which were referred to as the saline group, L group, **TB** NPs group, **TB** NPs + L(PDT) group (administered by **TB** NPs with laser illumination every interval of 30 s) and **TB** NPs + L group. Specially, the **TB** NPs + L(PDT) group was harnessed to measure the type I PDT efficacy. The total irradiation time for mice in L group, **TB** NPs + L(PDT) group and **TB** NPs + L group was 7 min (0.5 W cm^{-2}) after 8 h intravenous post-injection, respectively. When the tumors were about 100 mm^3, **TB** NPs (125 μL) or saline (400 μmol L^{-1}) were intravenously injected into each mouse, respectively. The length and width of tumors and body weight of each mouse were recorded every two days in two weeks. The mice were sacrificed after treatment and the tumors and main organs were collected.

RESULTS AND DISCUSSION

Characterization of TB

TB was first synthesized from an ethene-bridged BODIPY dimer *via* a palladium catalyzed C–H arylation with $C_{12}H_{25}$OTPE-Br (Schemes S1 and S2).

The molecular structure of **TB** was fully confirmed by ^{1}H NMR, ^{13}C NMR and MALDI-TOF MS (Figs S1–S6). The photophysical properties of **TB** were examined in various solvents and data are summarized in Table S1. As shown in Fig. 1a, the maximum absorption of **TB** was at 802 nm in toluene. The mass extinction coefficient of **TB** at 802 nm is 286.56 L g^{-1} cm^{-1}, which is much larger than that of most reported phototheranostic reagents, such as graphene oxide (3.6 L g^{-1} cm^{-1}) and black phosphorus quantum dots (14.8 L g^{-1} cm^{-1}) [60,61], suggesting the extremely strong NIR light-harvesting ability of **TB**. As a crucial element for phototheranostics, the photostability of **TB** was evaluated. From Fig. 1b, the maximum absorption of **TB** in *N*,*N*-dimethylformamide (DMF) decreased by less than 2% after 25 min continuous irradiation. As a striking contrast, the clinically phototheranostic reagent ICG was quickly degraded only after 3 min illumination (0.5 W cm^{-2}, Fig. S7). Moreover, the absorption spectrum of **TB** shows negligible change even when exposed to indoor light for one month (Fig. S8), which demonstrates the ultrahigh photostability of **TB** for further phototheranostic process. The fluorescence emission of **TB** was then characterized (Fig. 1c). **TB** displayed a deep NIR emission with the maximal peak at 851 nm and shoulder peak at 949 nm in toluene, 855 and 944 nm in dichloromethane (DCM), and 881 and 981 nm in acetonitrile (MeCN), respectively. Inspired by the specific molecular structure, **TB** was speculated to possess an outstanding ability to generate heat and reactive oxygen species (ROS) under irradiation. A continuous temperature rise was detected by using an IR thermal camera when **TB** was exposed to laser irradiation. Astoundingly, Fig. 1d reveals that the photoinitiated hyperthermia even when **TB** (50 μmol L^{-1}) in boiled DMF was continuously exposed to 808 nm illumination (1 W cm^{-2}), demonstrating the great potential of **TB** for further PTT against tumor. Then, the $^1O_2$ trap probe ABDA and the $O_2^{-\bullet}$ trap probe DHE were initially harnessed to explore the ROS type that **TB** generated under laser irradiation. Surprisingly, there was almost no degradation of ABDA in **TB** solution, confirming that **TB** could not produce $^1O_2$ (Fig. S9). However, the DHE fluorescence displayed a rapid increase under irradiation when the concentration of **TB** was only 10 μmol L^{-1} (Fig. 1e), amply verifying the strong $O_2^{-\bullet}$ generation capability. Furthermore, electron spin resonance (ESR) spectroscopy was carried out to confirm this hypothesis. It was clear that no ESR signals of $^1O_2$ could be found for **TB** solution after 10 min irradiation. However, after light irradiation, four characteristic peaks of $O_2^{-\bullet}$ (peak a, Fig. 1f) were clearly detected by using DMPO in ESR spectroscopy, further confirming that **TB** could effectively produce $O_2^{-\bullet}$ rather than $^1O_2$ under irradiation. It should be noted that due to the thermo-sensitivity of DMPO, three peaks representing the breakage of DMPO (peak b, Fig. 1f) in ESR spectroscopy were found for **TB** in both H_2O and DMSO solutions when exposed to laser illumination, verifying the strong hyperthermia generation capability of **TB**.

Theoretical calculation

Furthermore, density functional theory (DFT) and time dependent DFT (TDDFT) were carried out using the B3LYP functional and a 6-31G(d) basis set to understand

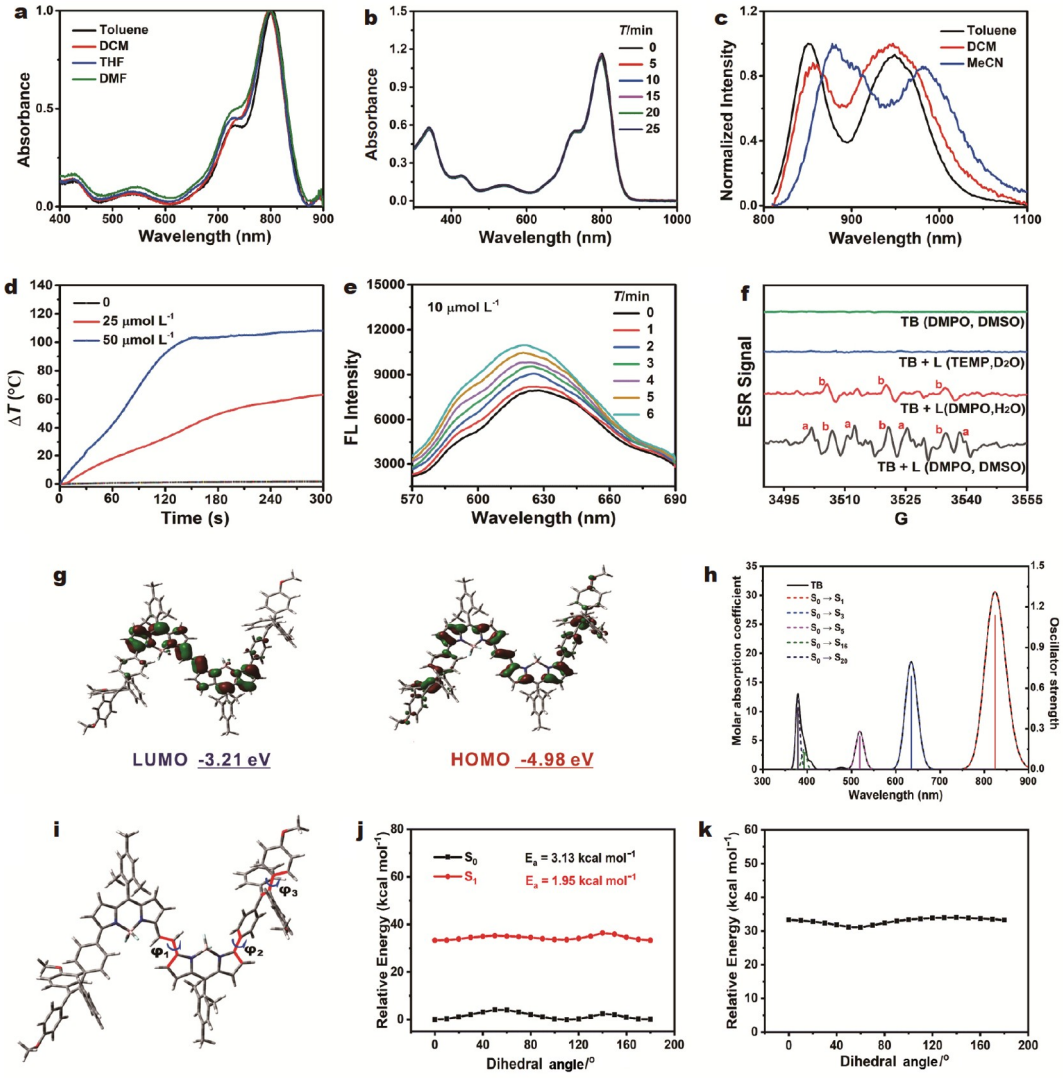

Figure 1 (a) Absorption spectra of **TB** in different solutions. (b) The photostability of **TB** under continuous 808 nm laser illumination (0.5 W cm^{-2}). (c) Normalized fluorescence emission spectra of **TB** in different solutions. (d) The raised temperature of **TB** under laser illumination (808 nm, 1 W cm^{-2}). (e) Fluorescence intensity change of $O_2^{-\bullet}$ probe triggered by **TB** under irradiation. (f) The ESR signals for $O_2^{-\bullet}$ and $^1O_2$ characterization (a: the characteristic peaks of $O_2^{-\bullet}$; b: the characteristic peaks of the breakage for DMPO caused by hyperthermia under irradiation). (g) The frontier MOs of the ground-state geometry for **TB**. (h) Calculated ultraviolet-visible (UV-vis) absorption of **TB**. The unit for molar absorption coefficient is 10^5 L mol^{-1} cm^{-1}. The mesitylene units and the long alkyl chains in the structure were omitted for clarity. (i) The dihedral angles of **TB**. (j) The energy levels of the S_0 (black) and S_1 (red) states of **TB** around the C–C bond with various dihedral angles $\varphi 2$. (k) The energy gap between the S_0 and S_1 states of **TB** around the C–C bond with various dihedral angles $\varphi 2$.

the excellent photophysical propoties of **TB** and calculation results are summarized in Fig. 1g, Fig. S10 and Table S2. The calculated highest occupied molecular orbitals (HOMO) energy levels were increased from −5.97 to −4.98 eV for **TB** when compared with the BODIPY core, while the lowest unoccupied molecular orbitals (LUMO) energy levels decreased from −2.84 to −3.21 eV. The TDDFT calculated parameter (Table S2) of **TB** shows the $S_0 \rightarrow S_1$ transition with an excitation energy at 823.56 nm. This excited state might contribute to the observed absorption of **TB** in the experiment. The TDDFT calculation in Fig. 1h also indicates that the absorption of **TB** corresponds to the $S_0 \rightarrow S_1$ transition which originated from HOMO to LUMO with the largest mass extinction coefficient, exhibiting a typical π-π* characteristics.

As shown in Fig. 1c, a larger bathochromic shift and dramatically decreased fluorescence (fluorescent quan-

tum yields from 0.1 to 0.01 in toluene and MeCN, respectively) were observed when the solvent polarity was increased (Table S1), which was highly in accordance with the typical intramolecular electron transfer process. The frontier molecule orbitals of the DFT calculations for **TB** in Fig. 1g also indicate the distinct electron donating from $C_{12}H_{25}$OTPE units to dimer BODIPY core. Considering both theoretical and experimental results, it was concluded that the strong $O_2^{-\bullet}$ generation of **TB** was attributed to the D-A-D molecular structure. Moreover, the dihedral angles for $\varphi 1$, $\varphi 2$ and $\varphi 3$ (Fig. 1i) in the optimized ground states were 179.02°, 143.62° and 166.88°, respectively, which firmly confirmed that **TB** owned a twisted molecular structure. In addition, due to the shielding effect of long alkyl chains in the $C_{12}H_{25}$OTPE unit, the intermolecular aggregation-caused $O_2^{-\bullet}$ quenching could be greatly reduced when **TB** was encapsulated into nano-assemblies.

Moreover, we speculated that the introduction of the $C_{12}H_{25}$OTPE unit to dimer BODIPY core might greatly endow **TB** with a superb photoinduced heat generation, since the TPE unit could be considered as the molecular rotor. Then, potential energy curves at both S_0 and S_1 states of **TB** at different dihedral angles were investigated. By comparing the potential energy curves of **TB** with different $\varphi 1$, $\varphi 2$ and $\varphi 3$ (Fig. 1j and Fig. S11), the non-radiative deactivation within rotations around $\varphi 2$ possessed the smallest E_{gap} in both ground state and first excited state, indicating that the rotation of the $C_{12}H_{25}$-OTPE around the dimer BODIPY core was dominant in **TB**. However, it was noted that the energy barrier of **TB** in $\varphi 2$ for S_0 was 3.13 kcal mol^{-1}, which was larger than that of S_1 (1.95 kcal mol^{-1}) (Fig. 1j), suggesting that the rotation tended to occur at the excited state. The excited rotation and small E_{gap} (shown in Fig. 1k) highly disclosed that the introduction of $C_{12}H_{25}$OTPE unit endowed **TB** with the excellent photothermal conversion property.

Characterization of TB NPs

To further enhance the solubility of **TB** in aqueous media, **TB** was then encapsulated by the block copolymer PEG_{45}-*b*-PLA_{24} to fabricate **TB** NPs. In order to characterize the morphology of **TB** NPs, transmission electron microscopy (TEM) was first used. From Fig. 2a, it was noted that **TB** NPs were dispersed well to form well-defined spherical self-assemblies with the average size around 90 nm. And the dynamic light scattering (DLS) result for size distribution in Fig. 2b was consistent with the TEM image, implying the potential of **TB** NPs for tumor accumulation. The photophysical properties of **TB** NPs were further explored. It was noted that the maximum absorption of **TB** NPs was around 810 nm which is very suitable for 808 nm light absorbing (Fig. 2c). **TB** NPs still possessed ultra-stable photostability, which was convinced by the faint change of absorption spectrum for **TB** NPs under 60 min laser irradiation (Fig. S12). Moreover, the fluorescence emission of **TB** NPs was evaluated. A deep NIR emission around 880 nm was observed and the relative fluorescence quantum yield of **TB** NPs was calculated as 0.77% (Fig. S13). Under 808 nm laser irradiation, **TB** NPs still possessed an $O_2^{-\bullet}$ generated capability with time elapsing (Fig. 2d, e), demonstrating that **TB** NPs has the potential to act as an $O_2^{-\bullet}$ photogenerator under the aqueous media in tumor. Moreover, since **TB** could efficiently raise the temperature in DMF, we supposed that **TB** NPs possessed an ultrahigh PCE under laser illumination as well. Then the increased temperature of **TB** NPs *versus* sample concentration (from 20 to 50 μmol L^{-1}) was examined under 0.5 W cm^{-2} laser power density (Fig. 2f). The increased temperature was about 60°C even at a concentration of **TB** NPs as low as only 20 μmol L^{-1}, indicating the strong photothermal effect of **TB** NPs for further usage to induce tumor cell ablation. In addition, when the laser power density changed to 1 W cm^{-2}, the solution temperature of **TB** NPs (50 μmol L^{-1}) raised up to 100°C after only 1.5 min irradiation (Fig. 2g), suggesting the strong photothermal conversion behavior of **TB** NPs. From Fig. 2h and Fig. S14, the PCE of **TB** NPs was 62%. In addition, repeated cycles of heating and cooling were carried out for **TB** NPs at the concentration of 50 μmol L^{-1} under laser irradiation (0.3 W cm^{-2}) to evaluate their photothermal stability. From Fig. 2h, it was noticed that the temperature elevation of the 4th cycle was remained almost the same level of the first cycle. Thus, the negligible attenuation of PCE demonstrated that **TB** NPs could bear repeated laser illumination. Photoacoustic (PA) performance of **TB** NPs was studied at different concentrations from 10 to 50 μmol L^{-1}. As shown in Fig. 2i, PA signals of **TB** NPs show a linear enhancement with the increased concentration, which is in agreement with the photothermal results. The above characteristics, including NIR-absorption, super photostability, superb $O_2^{-\bullet}$ generation and ultrahigh PCE, clearly demonstrate that **TB** NPs could act as an ideal phototherapeutic reagent for defeating tumor.

Cellular uptake and $O_2^{-\bullet}$ generation of TB NPs

In vitro cellular uptake of **TB** NPs was investigated *via* confocal laser scanning microscope (CLSM) after incubation of 4T1 murine breast cancer cells with **TB** NPs

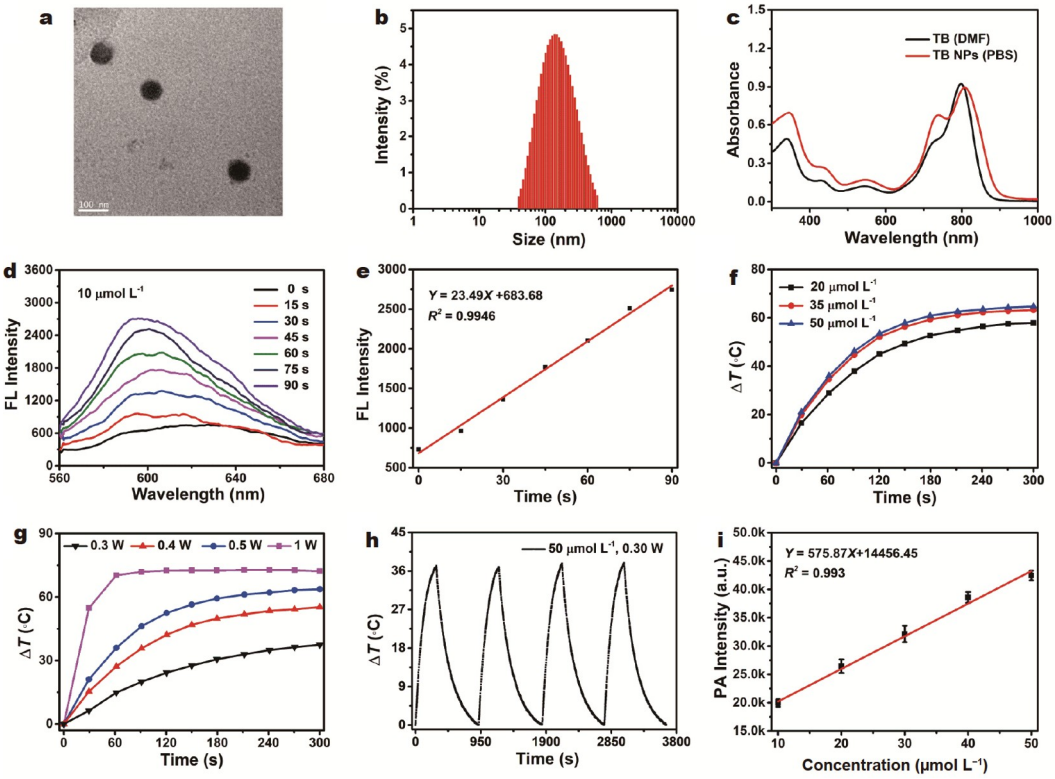

Figure 2 (a) TEM image of **TB** NPs. Scale bar: 100 nm. (b) Size distribution of **TB** NPs. (c) The absorption spectra of **TB** NPs after assembly. (d) Time-dependent fluorescence intensity changes of DHE for **TB** NPs (10 μmol L^{-1}) under laser illumination. (e) Plots of the fluorescence intensity change of DHE for **TB** NPs under irradiation. (f) Temperature changes of **TB** NPs at various concentrations (0.5 W cm^{-2}). (g) The raised temperature for **TB** NPs (50 μmol L^{-1}) under irradiation with different power densities. (h) Photothermal stability of **TB** NPs (50 μmol L^{-1}) during four cycles (0.3 W cm^{-2}). (i) PA signal intensities of **TB** NPs at different concentrations.

for different time. As illustrated in Fig. 3a, 4T1 cells treated with **TB** NPs displayed obviously red fluorescence after 4 h incubation, confirming that **TB** NPs could be efficiently internalized by 4T1 cells. The preferable endocytosis of **TB** NPs was highly favorable for causing subsequent photocytotoxicity. Since **TB** NPs exhibited remarkable $O_2^{-\bullet}$ and hyperthermia generation efficiency, a series of cell experiments were carried out to verify the phototherapeutic efficacy of **TB** NPs *in vitro*. As shown in Fig. 3b, flow cytometry analysis confirmed that **TB** NPs could generate the most ROS in cells after irradiation. CLSM images in Fig. S15 show the similar result as that in flow cytometry analysis. Moreover, three different ROS probes were harnessed to prove the $O_2^{-\bullet}$ generation ability of **TB** NPs in tumor cells under different cultivation conditions. After irradiation, bright red fluorescence of DHE assigned to $O_2^{-\bullet}$ was observed in 4T1 cells by CLSM under normoxia (Fig. 3c), implying **TB** NPs might show an efficient type I PDT efficacy against tumor cells. However, no $^1O_2$-related SOSG fluorescence was observed for cells incubated with **TB** NPs after 10 min irradiation (Fig. 3d), which matched well with the above results in Fig. S9 and Fig. 1f. Interestingly, green fluorescence of HPF representing the ·OH generation was detected for cells incubated with **TB** NPs under laser irradiation, which was attributed to the conversion of $O_2^{-\bullet}$ to ·OH under the intracellular SOD-mediated disproportionation reactions (Fig. 3e). Moreover, 4T1 cells were also cultivated under hypoxic condition (2% O_2). The remarkable DHE fluorescence could still be detected for cells in CLSM images after hypoxic treatment, implying **TB** NPs still possessed an $O_2^{-\bullet}$ generation performance under hypoxia.

Cytotoxicity of TB NPs

To demonstrate the phototherapeutic effect of **TB** NPs, MTT assays were employed. From Fig. 3f, there was unobvious toxicity to 4T1 cells without irradiation, suggesting the outstanding biosafety of **TB** NPs. To eliminate the interference of heat generation for fully evaluating PDT efficacy, cells incubated with **TB** NPs were exposed to 808 nm laser (0.1 W cm^{-2}) for every interval of 30 s,

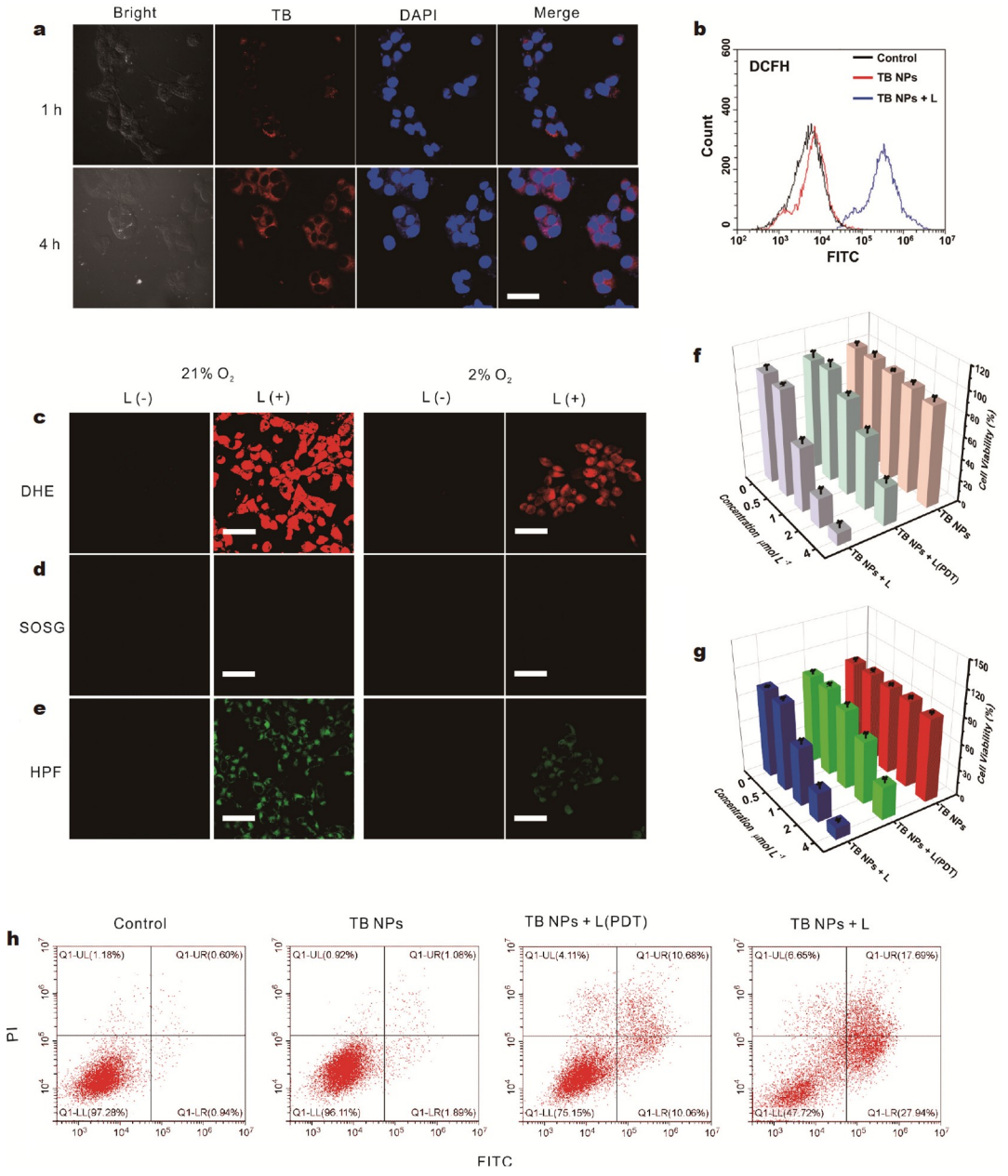

Figure 3 (a) Cell uptake of **TB** NPs. Scale bar: 50 μm. (b) Flow cytometry analysis of ROS generation in 4T1 cells. Intracellular (c) $O_2^{-\bullet}$, (d) $^1O_2$ and (e) ·OH production of 4T1 cells under normoxia (21% O_2) or hypoxia (2% O_2). Scale bars: 50 μm. (f) Cell viabilities of 4T1 cells under normoxia (21% O_2). (g) 4T1 cells treated with **TB** NPs under hypoxic condition (2% O_2). (h) Quantification of annexin V-FITC and PI double-labeled hypoxic 4T1 cells under different treatment.

since the raised temperature for **TB** NPs (50 μmol L^{-1}) was only 6°C after 30 s laser irradiation (0.3 W cm^{-2}). It was found that the cell viabilities continuously decreased with increased concentration of **TB** NPs under 808 nm laser illumination. Interestingly, regardless of the cell lines, when the cultivation concentration of **TB** NPs was 4 μmol L^{-1}, **TB** NPs showed high phototoxicities with the cell viabilities at 35.2% for 4T1 cells and 30.4% for MCF-7 cells (the total illumination time for both cell lines was 5 min), respectively. Notably, with continuous irradiation for 5 min, the 4T1 cell viability was quickly dropped to 27.2% and the viability of MCF-7 cells was detected at 27.2% when the concentration of **TB** NPs was only 2 μmol L^{-1} (Fig. S16). Moreover, when the cells were

cultivated under hypoxia, negligible difference of cell viabilities was also observed (Fig. 3g), which indicated the outstanding phototherapeutic efficacy of **TB** NPs to combat hypoxic tumor cells. Furthermore, FITC and PI were applied to explore the phototherapy efficacy of **TB** NPs in hypoxia. Likewise, the significantly increased cells in PI-positive region suggested that cell death was induced by the incubation with **TB** NPs under laser irradiation (Fig. 3h). Much more cell apoptosis was observed for **TB** NPs with continuous laser irradiation, which validated an excellent synergistic therapeutic efficiency of **TB** NPs towards hypoxic tumor cells.

In vivo bioimaging of TB NPs

Inspired by the excellent results *in vitro*, *in vivo* evaluation of phototherapy for **TB** NPs on 4T1 tumor-bearing mice was carried out. Considering that the relative fluorescence quantum yield of **TB** NPs was only 0.77%, 4T1-tumor bearing mice were intravenously injected with ICG-labeled **TB** NPs. The images were collected by a fluorescence imaging system. A gradually enhanced fluorescence signal in tumor was observed after 8 h injection, demonstrating that **TB** NPs were able to be effectively accumulated at tumor sites (Fig. 4a). Moreover, high PCE endowed **TB** NPs with strong photothermal imaging and PA imaging capabilities *in vivo*. In order to measure the *in vivo* photothermal imaging ability, mice were intravenously injected with **TB** NPs at two concentrations (10 and 50 μmol L^{-1}), respectively. After 8 h intravenous administration, mice were anesthetized and then tumors were illuminated by an 808 nm laser (0.5 W cm^{-2}). As expected, attributed to the ultrahigh

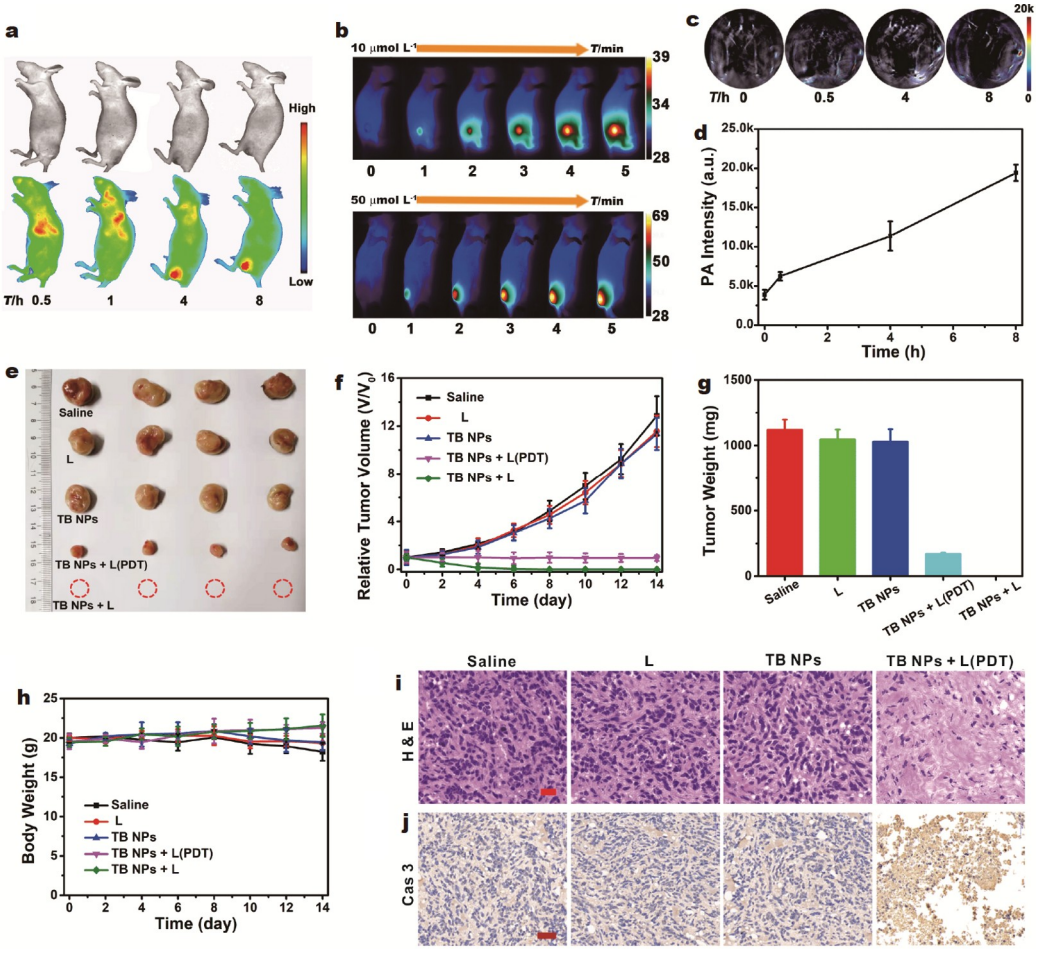

Figure 4 (a) *In vivo* fluorescence images of ICG-labeled **TB** NPs in tumor-bearing mice. (b) Photothermal images of mice after 8 h injection with **TB** NPs under laser illumination. (c) *In vivo* PA imaging of **TB** NPs. (d) The corresponding relative PA signal intensities of **TB** NPs *versus* different time on tumor. (e) Photographs of excised tumors for different groups. (f) Relative 4T1 tumor volume for different groups during therapy. (g) Tumor weight in different groups. (h) Body weight in different groups during phototherapy. (i) Hematoxylin-eosin (H&E) staining of tumors after different treatments. Scale bar: 20 μm. (j) Immunohistochemical analysis (cleaved Cas 3) in tumor after treatment. Scale bar: 50 μm.

PCE of **TB** NPs, the tumor temperature rapidly increased to about 40°C with the concentration of **TB** NPs at 50 μmol L^{-1} (Fig. 4b), implying the further PTT usage of **TB** NPs in tumor. Furthermore, *in vivo* PA imaging of **TB** NPs was evaluated by a noninvasive PA imaging system. After intravenous injection with **TB** NPs (125 μL, 50 μmol L^{-1}), the PA intensity at tumor was gradually enhanced as well (Fig. 4c). As shown in Fig. 4d, the PA intensity at 8 h was about 5-fold of the initial value, which showed the similar trend to the fluorescence imaging result. Consequently, **TB** NPs showed the capability to accumulate in tumor within 8 h.

In vivo antitumor efficacy of TB NPs

To quantitatively assess the antitumor efficacy, mice bearing 4T1 tumors were randomly assigned into five groups. According to the corresponding digital pictures (Fig. 4e), the average tumor volume in the saline group showed more than 12-fold increase of initial tumor volume, indicating negligible anticancer efficacy for saline to trigger tumor ablation (Fig. 4f). Moreover, the tumor growth in **TB** NPs group was similarly to that in the saline group, suggesting the negligible antitumor efficacies for **TB** NPs without laser irradiation. Comparatively, in **TB** NPs + L(PDT) group, effective tumor growth suppression was observed, which indicated the satisfactory type I PDT efficacy of **TB** NPs. Importantly, according to the changes of relative tumor volume over time, **TB** NPs with continuous 808 nm illumination resulted in completely tumor ablation and the tumor elimination rate reached 100%, demonstrating the outstanding synergistic type I PDT/PTT therapeutic efficacy in defeating tumor. Moreover, the tumor-weight records in Fig. 4g were highly consistent with the tumor volume growth curves. In addition, all mice exhibited unobvious body weight loss (Fig. 4h), implying that negligible side effects of **TB** NPs throughout the whole treatment period. Furthermore, histological analysis and immunohistochemical analysis were utilized to evaluate the treatment effect. Fig. 4i shows that the nuclei of tumor cells are almost unchanged in saline group, L group and **TB** NPs group without irradiation, while parts of the nuclei are distorted and even destroyed in the TB NPs + L (PDT) group. Moreover, considering that the level of cleaved Caspase 3 (Cas 3) is largely increased during cell apoptosis, the Cas 3 expression was further testified in different tested groups. In contrast to the low expression of cleaved Cas 3 in saline group, Cas 3 expression was significantly enhanced in **TB** NPs + L(PDT) group (Fig. 4j). This result gave further evidence that **TB** NPs under irradiation could activate the cleaved Cas 3 expression during type I PDT period. The H&E staining of main organs (hearts, spleens, livers, lungs and kidneys) in Fig. S17 shows that **TB** NPs caused no damage to normal tissues, indicating the outstanding phototoxicity and excellent biocompatibility of **TB** NPs.

CONCLUSIONS

In summary, we have developed a novel NIR-absorbing (802 nm) unimolecular $O_2^{-\bullet}$ and hyperthermia photogenerator (**TB**) to defeat hypoxic tumors. According to theoretical calculation, the twist D-A-D molecular structure and molecular rotation endowed **TB** with satisfactory $O_2^{-\bullet}$ and hyperthermia generation, respectively. The prepared **TB** NPs were found to exhibit excellent photothermal and PA signals due to their high PCE. Moreover, *in vivo* experiments disclosed that **TB** NPs showed outstanding phototherapeutic performances to induce tumor elimination under continuous laser irradiation. Therefore, this study would propose a new strategy for developing oxygen-independent phototherapeutic reagents to fight against hypoxic tumors.

Received 25 March 2021; accepted 10 May 2021; published online 29 July 2021

1 Minchinton AI, Tannock IF. Drug penetration in solid tumours. Nat Rev Cancer, 2006, 6: 583–592
2 Fan W, Huang P, Chen X. Overcoming the Achilles' heel of photodynamic therapy. Chem Soc Rev, 2016, 45: 6488–6519
3 Lv W, Zhang Z, Zhang KY, *et al.* A mitochondria-targeted photosensitizer showing improved photodynamic therapy effects under hypoxia. Angew Chem Int Ed, 2016, 55: 9947–9951
4 Fu LH, Qi C, Lin J, *et al.* Catalytic chemistry of glucose oxidase in cancer diagnosis and treatment. Chem Soc Rev, 2018, 47: 6454–6472
5 Xu J, Shi R, Chen G, *et al.* All-in-one theranostic nanomedicine with ultrabright second near-infrared emission for tumor-modulated bioimaging and chemodynamic/photodynamic therapy. ACS Nano, 2020, 14: 9613–9625
6 Feng L, Gai S, He F, *et al.* Multifunctional bismuth ferrite nanocatalysts with optical and magnetic functions for ultrasound-enhanced tumor theranostics. ACS Nano, 2020, 14: 7245–7258
7 Moen I, Stuhr LEB. Hyperbaric oxygen therapy and cancer—A review. Targ Oncol, 2012, 7: 233–242
8 Liang X, Chen M, Bhattarai P, *et al.* Perfluorocarbon@porphyrin nanoparticles for tumor hypoxia relief to enhance photodynamic therapy against liver metastasis of colon Cancer. ACS Nano, 2020, 14: 13569–13583
9 Wang C, Sun X, Cheng L, *et al.* Multifunctional theranostic red blood cells for magnetic-field-enhanced *in vivo* combination therapy of cancer. Adv Mater, 2014, 26: 4794–4802
10 Gao C, Lin Z, Wang D, *et al.* Red blood cell-mimicking micromotor for active photodynamic cancer therapy. ACS Appl Mater Interfaces, 2019, 11: 23392–23400
11 Zhang S, Li Q, Yang N, *et al.* Phase-change materials based na-

noparticles for controlled hypoxia modulation and enhanced phototherapy. Adv Funct Mater, 2019, 29: 1906805
12 Liu L, He H, Luo Z, *et al. In situ* photocatalyzed oxygen generation with photosynthetic bacteria to enable robust immunogenic photodynamic therapy in triple-negative breast cancer. Adv Funct Mater, 2020, 30: 1910176
13 Fu LH, Wan Y, Li C, *et al.* Biodegradable calcium phosphate nanotheranostics with tumor-specific activatable cascade catalytic reactions-augmented photodynamic therapy. Adv Funct Mater, 2021, 31: 2009848
14 Yu Q, Huang T, Liu C, *et al.* Oxygen self-sufficient NIR-activatable liposomes for tumor hypoxia regulation and photodynamic therapy. Chem Sci, 2019, 10: 9091–9098
15 Liu C, Cao Y, Cheng Y, *et al.* An open source and reduce expenditure ROS generation strategy for chemodynamic/photodynamic synergistic therapy. Nat Commun, 2020, 11: 1735
16 Liu C, Xing J, Akakuru OU, *et al.* Nanozymes-engineered metal-organic frameworks for catalytic cascades-enhanced synergistic cancer therapy. Nano Lett, 2019, 19: 5674–5682
17 Li W, Zhong D, Hua S, *et al.* Biomineralized biohybrid algae for tumor hypoxia modulation and cascade radio-photodynamic therapy. ACS Appl Mater Interfaces, 2020, 12: 44541–44553
18 Wang YG, Zhan YP, Pan SY, *et al.* Hyperbaric oxygen promotes malignant glioma cell growth and inhibits cell apoptosis. Oncology Lett, 2015, 10: 189–195
19 Wang Z, Jia T, Sun Q, *et al.* Construction of Bi/phthalocyanine manganese nanocomposite for trimodal imaging directed photodynamic and photothermal therapy mediated by 808 nm light. Biomaterials, 2020, 228: 119569
20 Ma P', Xiao H, Yu C, *et al.* Enhanced cisplatin chemotherapy by iron oxide nanocarrier-mediated generation of highly toxic reactive oxygen species. Nano Lett, 2017, 17: 928–937
21 Dai Y, Cheng S, Wang Z, *et al.* Hypochlorous acid promoted platinum drug chemotherapy by myeloperoxidase-encapsulated therapeutic metal phenolic nanoparticles. ACS Nano, 2018, 12: 455–463
22 Chen D, Wang Z, Dai H, *et al.* Boosting $O_2^{\bullet-}$ photogeneration *via* promoting intersystem-crossing and electron-donating efficiency of aza-BODIPY-based nanoplatforms for hypoxic-tumor photodynamic therapy. Small Methods, 2020, 4: 2000013
23 Li M, Xia J, Tian R, *et al.* Near-infrared light-initiated molecular superoxide radical generator: Rejuvenating photodynamic therapy against hypoxic tumors. J Am Chem Soc, 2018, 140: 14851–14859
24 Beissenhirtz MK, Scheller FW, Viezzoli MS, *et al.* Engineered superoxide dismutase monomers for superoxide biosensor applications. Anal Chem, 2006, 78: 928–935
25 Chen XJ, West AC, Cropek DM, *et al.* Detection of the superoxide radical anion using various alkanethiol monolayers and immobilized cytochrome *c*. Anal Chem, 2008, 80: 9622–9629
26 Huang Y, You X, Wang L, *et al.* Pyridinium-substituted tetraphenylethylenes functionalized with alkyl chains as autophagy modulators for cancer therapy. Angew Chem Int Ed, 2020, 59: 10042–10051
27 Li M, Shao Y, Kim JH, *et al.* Unimolecular photodynamic O_2-economizer to overcome hypoxia resistance in phototherapeutics. J Am Chem Soc, 2020, 142: 5380–5388
28 Chen D, Yu Q, Huang X, *et al.* A highly-efficient type I photosensitizer with robust vascular-disruption activity for hypoxic-and-metastatic tumor specific photodynamic therapy. Small, 2020, 16: 2001059
29 Chang FP, Chen YP, Mou CY. Intracellular implantation of enzymes in hollow silica nanospheres for protein therapy: Cascade system of superoxide dismutase and catalase. Small, 2014, 10: 4785–4795
30 Zhang Y, Wang F, Liu C, *et al.* Nanozyme decorated metal-organic frameworks for enhanced photodynamic therapy. ACS Nano, 2018, 12: 651–661
31 Li Y, Zhang W, Niu J, *et al.* Mechanism of photogenerated reactive oxygen species and correlation with the antibacterial properties of engineered metal-oxide nanoparticles. ACS Nano, 2012, 6: 5164–5173
32 Dai Y, Yang Z, Cheng S, *et al.* Toxic reactive oxygen species enhanced synergistic combination therapy by self-assembled metal-phenolic network nanoparticles. Adv Mater, 2018, 30: 1704877
33 Wang M, Hou Z, Al Kheraif AA, *et al.* Mini review of TiO_2-based multifunctional nanocomposites for near-infrared light-responsive phototherapy. Adv Healthcare Mater, 2018, 7: 1800351
34 Bu Y, Xu T, Zhu X, *et al.* A NIR-I light-responsive superoxide radical generator with cancer cell membrane targeting ability for enhanced imaging-guided photodynamic therapy. Chem Sci, 2020, 11: 10279–10286
35 Gurram B, Li M, Li M, *et al.* NIR-excited superoxide radical procreators to eradicate tumors by targeting the lyso-membrane. J Mater Chem B, 2019, 7: 4440–4450
36 Wan Q, Zhang R, Zhuang Z, *et al.* Molecular engineering to boost AIE-active free radical photogenerators and enable high-performance photodynamic therapy under hypoxia. Adv Funct Mater, 2020, 30: 2002057
37 Wu M, Liu Z, Zhang W. An ultra-stable bio-inspired bacteriochlorin analogue for hypoxia-tolerant photodynamic therapy. Chem Sci, 2021, 12: 1295–1301
38 Xie Z, Fan T, An J, *et al.* Emerging combination strategies with phototherapy in cancer nanomedicine. Chem Soc Rev, 2020, 49: 8065–8087
39 Ou H, Li J, Chen C, *et al.* Organic/polymer photothermal nanoagents for photoacoustic imaging and photothermal therapy *in vivo*. Sci China Mater, 2019, 62: 1740–1758
40 Liu Y, Wang H, Li S, *et al. In situ* supramolecular polymerization-enhanced self-assembly of polymer vesicles for highly efficient photothermal therapy. Nat Commun, 2020, 11: 1724
41 Dong T, Wen K, Chen J, *et al.* Significant enhancement of photothermal and photoacoustic efficiencies for semiconducting polymer nanoparticles through simply molecular engineering. Adv Funct Mater, 2018, 28: 1800135
42 Yang T, Liu L, Deng Y, *et al.* Ultrastable near-infrared conjugated-polymer nanoparticles for dually photoactive tumor inhibition. Adv Mater, 2017, 29: 1700487
43 Abbas M, Zou Q, Li S, *et al.* Self-assembled peptide- and protein-based nanomaterials for antitumor photodynamic and photothermal therapy. Adv Mater, 2017, 29: 1605021
44 Zou Q, Abbas M, Zhao L, *et al.* Biological photothermal nanodots based on self-assembly of peptide-porphyrin conjugates for antitumor therapy. J Am Chem Soc, 2017, 139: 1921–1927
45 Li X, Liu L, Li S, *et al.* Biodegradable π-conjugated oligomer nanoparticles with high photothermal conversion efficiency for cancer theranostics. ACS Nano, 2019, 13: 12901–12911
46 Liu S, Zhou X, Zhang H, *et al.* Molecular motion in aggregates: Manipulating TICT for boosting photothermal theranostics. J Am Chem Soc, 2019, 141: 5359–5368
47 Zhao Z, Chen C, Wu W, *et al.* Highly efficient photothermal na-

noagent achieved by harvesting energy *via* excited-state intramolecular motion within nanoparticles. Nat Commun, 2019, 10: 768
48 Zhang R, Duan Y, Liu B. Recent advances of AIE dots in NIR imaging and phototherapy. Nanoscale, 2019, 11: 19241–19250
49 Ni JS, Zhang X, Yang G, *et al.* A photoinduced nonadiabatic decay-guided molecular motor triggers effective photothermal conversion for cancer therapy. Angew Chem Int Ed, 2020, 59: 11298–11302
50 Xi D, Xiao M, Cao J, *et al.* NIR light-driving barrier-free group rotation in nanoparticles with an 88.3% photothermal conversion efficiency for photothermal therapy. Adv Mater, 2020, 32: 1907855
51 Sun M, Yang D, Fanqi W, *et al.* SiO_2@Cu_7S_4 nanotubes for photo/chemodynamic and photo-thermal dual-mode synergistic therapy under 808 nm laser irradiation. J Mater Chem B, 2020, 8: 5707–5721
52 Feng J, Yu W, Xu Z, *et al.* An intelligent ZIF-8-gated polydopamine nanoplatform for *in vivo* cooperatively enhanced combination phototherapy. Chem Sci, 2020, 11: 1649–1656
53 Jiang F, Ding B, Zhao Y, *et al.* Biocompatible CuO-decorated carbon nanoplatforms for multiplexed imaging and enhanced antitumor efficacy *via* combined photothermal therapy/chemodynamic therapy/chemotherapy. Sci China Mater, 2020, 63: 1818–1830
54 Liu X, Jia HR, Zhu YX, *et al.* Mitochondrion- and nucleus-acting polymeric nanoagents for chemo-photothermal combination therapy. Sci China Mater, 2020, 63: 851–863
55 Wang K, Tu Y, Yao W, *et al.* Size-switchable nanoparticles with self-destructive and tumor penetration characteristics for site-specific phototherapy of cancer. ACS Appl Mater Interfaces, 2020, 12: 6933–6943
56 Zhang Z, Xu W, Kang M, *et al.* An all-round athlete on the track of phototheranostics: Subtly regulating the balance between radiative and nonradiative decays for multimodal imaging-guided synergistic therapy. Adv Mater, 2020, 32: 2003210
57 Wang Y, Gong N, Li Y, *et al.* Atomic-level nanorings (A-NRs) therapeutic agent for photoacoustic imaging and photothermal/photodynamic therapy of cancer. J Am Chem Soc, 2020, 142: 1735–1739
58 Zhao X, Long S, Li M, *et al.* Oxygen-dependent regulation of excited-state deactivation process of rational photosensitizer for smart phototherapy. J Am Chem Soc, 2020, 142: 1510–1517
59 Han X, Chen D, Sun J, *et al.* A novel cabazitaxel-loaded polymeric micelle system with superior *in vitro* stability and long blood circulation time. J Biomater Sci Polym Ed, 2016, 27: 626–642
60 Sun Z, Xie H, Tang S, *et al.* Ultrasmall black phosphorus quantum dots: Synthesis and use as photothermal agents. Angew Chem Int Ed, 2015, 54: 11526–11530
61 Robinson JT, Tabakman SM, Liang Y, *et al.* Ultrasmall reduced graphene oxide with high near-infrared absorbance for photothermal therapy. J Am Chem Soc, 2011, 133: 6825–6831

Acknowledgements This work was supported by the National Natural Science Foundation of China (21875063 and 21871006), the Science and Technology Commission of Shanghai Municipality for Shanghai International Cooperation Program (19440710600), and the Open Funding Project of the State Key Laboratory of Bioreactor Engineering.

Author contributions Zhu Y, Wu Q, Hao E, and Zhang W conceived and designed the project; Zhu Y and Wu Q analyzed the data; Chen C, Yang G contributed to the cell and animal experiments; Zhu Y and Wu Q wrote the paper with the support from Cao H and Gao Y; Jiao L, Hao E and Zhang W provided the technical support. All authors have given approval to the final version of the manuscript.

Conflict of interest The authors declare that they have no conflict of interest.

Supplementary information Experimental details and supporting data are available in the online version of the paper.

Weian Zhang is a full professor in polymer science at the East China University of Science and Technology. He received his PhD degree from the University of Science and Technology of China (USTC) in 2003. Prior to his independent work, he worked at the University of Bayreuth in Germany as a Humboldt fellow and the University of Leeds in UK as a Marie Curie fellow. His research interests concern preparation, self-assembly and application of photosensitive polymers.

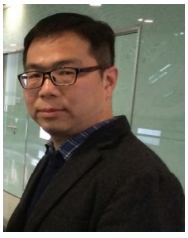

Erhong Hao joined Anhui Normal University after he received his PhD degree from Louisiana State University in 2007. He also received a Master's degree at USTC and a Bachelor's degree from Shandong University. He has been a full professor at the College of Chemistry and Materials Science since 2009. His research focuses on developing new fluorescent dyes and their applications as smart molecular probes, advanced imaging reagents and photosensitizers.

Lijuan Jiao received her Bachelor's degree (2000) from Shandong University, China, and her Master's degree (2003) from USTC. She obtained her PhD degree (2007) from Louisiana State University (USA). She joined Anhui Normal University in 2008, and became a full professor (2010) at the College of Chemistry and Materials Science. Her research focuses on the development of novel BODIPY and porphyrin-related dyes, understanding their photophysical properties and studying their optoelectrical and biological applications. She received an SPP/JPP Young Investigator Award for her research in BODIPY and oligopyrrole chemistry in 2016.

Yucheng Zhu received his BA degree from the East China University of Science and Technology, in 2016. He is a doctoral candidate under the supervision of Prof. Weian Zhang and Prof. Yun Gao at the East China University of Science and Technology. His current research interest focuses on the phototherapy of functional photosensitizers.

Qinghua Wu received his PhD degree under the supervision of Prof. Lijuan Jiao from Anhui Normal University, China, in 2019. He is now a postdoctoral fellow at Anhui Normal University. His current research interests focus on the design and synthesis of fluorescent dyes, their photophysical properties and biological applications.

具有扭曲D-A-D转子结构的近红外光疗试剂能够同时产生超氧自由基和光热用于消除乏氧肿瘤

朱玉呈[1†], 吴清华[2†], 陈超[1], 杨国梁[1], 曹红亮[1], 杲云[1], 焦莉娟[2*], 郝二宏[2*], 张伟安[1*]

摘要 肿瘤乏氧微环境严重抑制了肿瘤化疗、放疗及II型光动力治疗的疗效. 因此, 开发非氧气依赖性的肿瘤治疗方式具有重要意义. 在此, 我们设计了一种超稳定的近红外吸收的光热和超氧自由基($O_2^{-\bullet}$)供体(**TB**). 由于D-A-D分子结构, 在808 nm激光照射下, **TB**能够产生大量$O_2^{-\bullet}$. 此外, 由于电子供体同时还充当了转子基元, **TB**还能够在连续激光照射下产生极强的光热. 为了将**TB**应用于乏氧肿瘤治疗, **TB**被嵌段共聚物PEG_{45}-*b*-PLA_{24}封装以制成纳米颗粒(**TB** NPs). 扭曲的分子结构和长烷基链的屏蔽效应有效降低了组装体由于聚集所导致的$O_2^{-\bullet}$淬灭. 组装而成的**TB** NPs仍具有令人满意的$O_2^{-\bullet}$生成能力和较高的光热转化效率, 因而**TB** NPs可被用于乏氧肿瘤治疗. 此外, 由于**TB** NPs的光热转换效率较高, 其可被用于光声成像和光热成像. 在活体抗肿瘤实验中, 通过连续光照, **TB** NPs可以完全消除乏氧肿瘤. 本研究为设计非氧依赖性的光疗试剂用于乏氧肿瘤治疗提供了一种全新的策略.

